AGU PUBLICATIONS

JGR

Journal of Geophysical Research: Space Physics

RESEARCH ARTICLE

10.1002/2013JA019621

Key Points:
- We show a method for estimating vector neutral wind profiles from Arecibo data
- The method fully utilizes dual-beam ISR data taken during azimuth swings
- The profiles are broadly consistent with gravity waves but are impulsive

Correspondence to:
D. L. Hysell,
dlh37@cornell.edu

Citation:
Hysell, D. L., M. F. Larsen, and M. P. Sulzer (2014), High time and height resolution neutral wind profile measurements across the mesosphere/lower thermosphere region using the Arecibo incoherent scatter radar, *J. Geophys. Res. Space Physics*, *119*, 2345–2358, doi:10.1002/2013JA019621.

Received 13 NOV 2013
Accepted 7 MAR 2014
Accepted article online 12 MAR 2014
Published online 31 MAR 2014

High time and height resolution neutral wind profile measurements across the mesosphere/lower thermosphere region using the Arecibo incoherent scatter radar

D. L. Hysell[1], M. F. Larsen[2], and M. P. Sulzer[3]

[1]Earth and Atmospheric Sciences, Cornell University, Ithaca, New York, USA, [2]Physics and Astronomy, Clemson University, Clemson, South Carolina, USA [3]Arecibo Radio Observatory, Arecibo, Puerto Rico

Abstract A method for estimating the vector neutral wind profiles in the mesosphere and lower thermosphere (MALT) region of the upper atmosphere from Arecibo dual-beam incoherent scatter radar data is presented. The method yields continuous estimates of both the altitude-averaged *F* region plasma drifts and all three components of the altitude-resolved neutral wind profiles in the MALT using data taken while the Arecibo feed system swings in azimuth. The problem is mixed determined, and its solution is not inherently unique. Second-order Tikhonov regularization is used to find solutions consistent with the available data while being minimally structured, additional structure being unsupported by the data. The solution is found using the method of conjugate gradient least squares and sparse matrix mathematics. Example data acquired during an interval of midlatitude spread *F* are used to illustrate the method. The estimated wind profiles exhibit characteristics broadly consistent with gravity waves but are impulsive, with features that generally persist for less than one and a half wave periods.

1. Introduction

Among the most important state parameters for the study of the mesosphere and lower thermosphere (MALT) region are the neutral wind velocities. The winds are indicators of large-scale circulation in the upper atmosphere, of energy and momentum being transported across it by waves, and of the overall dynamical stability. Winds can be measured accurately in the MALT using chemical releases and by high-power Doppler lidar [e.g., *Larsen*, 2002; *Zhao et al.*, 2003; *Chu et al.*, 2005]. The relative ease of accessibility and geographic diversity of the world's incoherent scatter radars (ISRs), deployed at low, middle, and high latitudes on several continents, makes them attractive instruments for MALT wind observations as well. However, complications arise since it is the ionized rather than the neutral gas motion that the radars observe directly, and a number of different techniques appropriate for different altitude regimes have been applied to the neutral wind problem. The purpose of this paper is to describe a new method for estimating vector neutral winds in the MALT using the Arecibo radio telescope, the most sensitive of the ISRs. As Arecibo can only observe drifts in two coplanar directions at a time, statistical inference is a necessary component of the technique.

In fact, Arecibo has been making wind measurements in the MALT for quite a few years. Most of the important principles involved are discussed by *Harper* [1977, and references therein]. In the ionosphere, the neutral wind in the direction parallel to the geomagnetic field is a calculable function of the parallel-to-B ion drift speed. Below about 170 km, the two speeds are essentially equivalent, while above this, ion diffusion must also be considered and accounted for [*Vasseur*, 1969; *Behnke and Kohl*, 1974]. By measuring line of sight ion drifts with two beams in the magnetic meridional plane and assuming horizontal invariance, it is possible to isolate the parallel-to-B ion drift component and to estimate the associated neutral wind component. With the assumption that the vertical neutral wind is small, the meridional wind profile can thus be calculated.

The relationship between ion drifts perpendicular to B and the winds is more complicated, and winds can only be estimated from incoherent scatter below about 130 km where the ions are unmagnetized [*Harper et al.*, 1976]. An estimate of the perpendicular-to-B electric field is required to separate the Pedersen and Hall drift components from the measured ion drifts and to isolate the contribution due to neutral winds. The required *E* field estimate can be formulated on the basis of ion drifts measured in the fully magnetized *F*

region along three or more noncoplanar bearings, assuming spatial homogeneity and efficient electric field mapping along magnetic field lines [e.g., *Behnke and Harper*, 1973].

Estimating neutral winds in the perpendicular-to-B direction also requires a specification of the composition and the ion-neutral collision frequency for each important ion species. In practice, isomorphism in the incoherent scatter spectrum makes it impractical to estimate temperature, composition, and collisionality by fitting range-gated ISR data, even below 130 km altitude where the electron and ion temperatures are approximately equal. Modeling is generally incorporated in this aspect of the methodology. Below about 110 km altitude, however, the collisional coupling between ions and neutrals is strong, and ion and neutral drift velocities can be regarded as being essentially equivalent.

Variations of one aspect or another of the Harper methodology have been employed by numerous investigators for wind and wave studies in the midlatitude MALT region [e.g., *Burnside et al.*, 1983; *Roper et al.*, 1993; *Aponte et al.*, 2005; *Gong et al.*, 2012; *Huang et al.*, 2012]. These include studies that focus on the mesosphere, where the procedure is especially straightforward [*Mathews et al.*, 1981; *Rottger et al.*, 1981; *Fukao et al.*, 1982, 1985; *Rottger et al.*, 1983; *Tsuda et al.*, 1985; *Maekawa et al.*, 1986; *Zhou and Morton*, 2006]. The techniques and related databases have become sufficiently reliable to support studies of long-term trends over Arecibo [*Maekawa et al.*, 1987; *Tepley et al.*, 2011; *Santos et al.*, 2011; *Brum et al.*, 2012].

Harper [1977] utilized a multipulse pattern to make range-resolved autocorrelation function measurements in the *E* region and a long-pulse pattern to make accurate line of sight velocity measurements in the *F* region. Contemporary experiments at Arecibo have replaced the multipulse mode with a coded long pulse (CLP) and the long pulse with a multifrequency mode (MRACF) (see *Sulzer* [1986a, 1986b] for details). The new pulsing schemes exploit the capabilities of the Arecibo Observatory more fully than the old ones.

Wind measurements at Arecibo have generally been based on ISR data collected with either a single beam or with two coplanar beams directed at fixed azimuths. The fixed-azimuth approach is somewhat inefficient, however, since time spent during beam swinging maneuvers is wasted. Moreover, there is an implicit assumption that the winds and electric fields in the upper atmosphere are invariant during the time that it takes to acquire data and swing the beam. In view of the slow slew rate of the Arecibo beam system, this assumption may not be difficult to violate. *Sulzer et al.* [2005] introduced a novel refinement, incorporating statistical inverse theory in the estimation of *F* region plasma drifts from data taken when the beam was continuously swinging. In this paper, we generalize the result and apply a related technique to the entire horizontal wind estimation problem. The current work is an expansion of the more basic technique reported on by *Hysell et al.* [2009]. It bears some similarities to the work of *Nygrén et al.* [2011] except that we treat the underdetermined problem using a damped least squares approach, whereas they treated the even-determined or overdetermined problem using least squares. The analysis will require validation in the future to gain confidence in the output of the wind estimation technique, but in principle, it can yield profiles of all three wind components with a time resolution on the order of a minute and a height resolution of 300 m, which compares favorably with the measurement capabilities of the high-power lidar systems that are currently being used for mesosphere and lower thermosphere measurements. In addition, the ISR wind estimates extend to altitudes of 120 to 130 km.

2. Methodology

Here we describe a method to infer the vector neutral winds in the MALT region from Arecibo dual-beam incoherent scatter data. Ionospheric electric fields are estimated on the basis of *F* region incoherent scatter ion line line-of-sight drift measurements made using the MRACF mode [*Sulzer*, 1986a], which are averaged over all *F* region altitudes. Wind estimates are derived using *E* region incoherent scatter ion line line-of-sight drift measurements made using the coded long-pulse (CLP) mode [*Sulzer*, 1986b], which are range resolved. (The range resolution of the CLP data used here is 300 m.) The aforementioned electric field estimates are incorporated into the procedure for estimating winds. Information about ion composition is also required and is extracted from CLP autocorrelation function estimates through an iterative fitting procedure that involves a simple modeling component. The cadence of the experimental results is approximately once per minute.

Throughout the subsequent discussion, we make use of the language and formalism of statistical inverse theory as presented by *Menke* [1984], *Tarantola* [1987], and *Aster et al.* [2005].

2.1. Electric Field Estimates

Ion drift measurements in the *F* region ionosphere contain information about the transverse electric field. We regard this field to be essentially invariant throughout the *F* region and combine measurements from different range gates to improve statistical accuracy. Extracting electric field information entails performing some coordinate transformations and then implementing an inverse method.

The line of sight *F* region drifts measurements acquired with the line feed and Gregorian beam systems at Arecibo can be related to drifts in a geographic Cartesian (up-east-north) coordinate system with the assumption of spatial homogeneity through the linear transformation:

$$\begin{pmatrix} v_l \\ v_g \end{pmatrix} = \underbrace{\begin{pmatrix} 1 & 0 & 0 \\ c\theta & s\phi s\theta & c\phi s\theta \end{pmatrix}}_{Q} \begin{pmatrix} v_u \\ v_e \\ v_n \end{pmatrix} \tag{1}$$

where θ and ϕ are the azimuth and zenith angles of the Gregorian feed. (The line feed is taken to point toward zenith, although a more generalized form of (1) could be formulated trivially.) Of all the angles used in this analysis, only θ varies in time in practice. We use "s" and "c" as shorthand for sin and cosine.

More useful for the analysis than the geographic coordinate system is a Cartesian system aligned with the geomagnetic field. We define a right-handed system with a component parallel to $\mathbf{B}$, a component perpendicular to $\mathbf{B}$ in the horizontal plane, and another perpendicular component in the plane of the magnetic meridian. The components of the velocity in this system ($v_\parallel$, $v_{\perp e}$, $v_{\perp n}$) are related to the components in geographic coordinates through the transformation:

$$\begin{pmatrix} v_\parallel \\ v_{\perp e} \\ v_{\perp n} \end{pmatrix} = \underbrace{\begin{pmatrix} c\xi & s\eta s\xi & c\eta s\xi \\ 0 & c\eta & -s\eta \\ s\xi & -s\eta c\xi & -c\eta c\xi \end{pmatrix}}_{R^{-1}} \begin{pmatrix} v_u \\ v_e \\ v_n \end{pmatrix} \tag{2}$$

where η and ξ are the zenith and azimuth angles of the magnetic field, respectively. The transformation above can be inverted, yielding

$$\begin{pmatrix} v_u \\ v_e \\ v_n \end{pmatrix} = \underbrace{\begin{pmatrix} c\xi & 0 & s\xi \\ s\eta s\xi & c\eta & -s\eta c\xi \\ c\eta s\xi & -s\eta & -c\eta c\xi \end{pmatrix}}_{R} \begin{pmatrix} v_\parallel \\ v_{\perp e} \\ v_{\perp n} \end{pmatrix} \tag{3}$$

All together, the measured line of sight drifts can then be related to the drifts in magnetic coordinates with the definition of the transformation matrix $S \in \mathbb{R}^{2\times 3} = QR$. The nonzero elements of S are given by:

$$\begin{aligned} S_{11} &= c\xi \\ S_{12} &= 0 \\ S_{13} &= s\xi \\ S_{21} &= c\theta c\xi + s\theta s\xi (s\phi s\eta + c\phi c\eta) \\ S_{22} &= s\theta (s\phi c\eta - c\phi s\eta) \\ S_{23} &= c\theta s\xi - s\theta c\xi (s\phi s\eta + c\phi c\eta) \end{aligned}$$

such that

$$\begin{pmatrix} v_l \\ v_g \end{pmatrix} = S \begin{pmatrix} v_\parallel \\ v_{\perp e} \\ v_{\perp n} \end{pmatrix} \tag{4}$$

The preceding analysis accommodated a single pair of line of sight drift measurements acquired at a single time. For n measurements acquired at n distinct times, the resulting $2n$ data are related to the corresponding $3n$ drift components by

$$\begin{pmatrix} v_{l1} \\ v_{g1} \\ \vdots \\ v_{ln} \\ v_{gn} \end{pmatrix} = \underbrace{\begin{pmatrix} S_1 & & \\ & \ddots & \\ & & S_n \end{pmatrix}}_{T \in \mathbb{R}^{2n \times 3n}} \begin{pmatrix} v_{\parallel 1} \\ v_{\perp e1} \\ v_{\perp n1} \\ \vdots \\ v_{\parallel n} \\ v_{\perp en} \\ v_{\perp nn} \end{pmatrix} \tag{5}$$

where the subscripts refer to time steps and all the drifts measurements are taken to be independent.

The transformation in (5) has the form of the standard forward problem $d = Gm$, d being the data, the dual-beam drift velocity measurements at n different times in this case, m being the model parameters or state, the underlying vector drifts in a magnetic coordinate system, and "G" being the calculable, time-dependent linear system that transforms from one to the other. The matrix T is not square, the inverse problem is underdetermined, and the model parameters m cannot be found uniquely on the basis of the given data d as written. In order to proceed, we pose the inverse problem as an optimization problem, where additional penalties are introduced to reduce the solution space of m, creating a unique solution.

Applying the method of weighted, damped least squares, we seek a solution for m that minimizes the weighted forward prediction error with an added damping factor representing the additional penalty:

$$m = \underset{m}{\operatorname{argmin}} (Gm - d)^t W_d (Gm - d) + \alpha^2 m^t W_m m \tag{6}$$

where W_d is the inverse data error covariance matrix and W_m is a model weight matrix. If W_m is made to be the identity matrix, then the damping term plays the role of minimizing the model length, which can be interpreted as an implementation of Occam's razor. Other choices for W_m can be used to minimize the global first or second derivative (the roughness) of the model parameters. These choices are tantamount to performing zeroth-, first-, or second-order Tikhonov regularization in time. We employ second-order Tikhonov regularization here as a penalty for spurious temporal fluctuations that cannot be supported by the data. The α term is a regularization parameter which balances the impacts of the penalties.

Using the method of normal equations, it is easy to show that the inverse operator that satisfies the optimization equation is given by the weighted-damped least squares operator

$$\hat{G}^{-1} = (G^t W_d G + \alpha^2 W_m)^{-1} G^t W_d \tag{7}$$

$$m \approx \hat{G}^{-1} d \tag{8}$$

Applying the operator above to the data yields estimates of the vector ion drifts in a magnetic coordinate system at different times. The transverse components of the drifts are indicative of $\mathbf{E} \times \mathbf{B}$ drifts. The parallel component is not of interest to the present analysis and can be discarded.

2.2. Neutral Wind Profile Estimates

In the E region ionosphere/ lower thermosphere, ion drift measurements are indicative of electric fields and neutral winds. As with the electric fields, estimating the neutral winds from the measurements involves a series of coordinate transformations followed by an inverse method. It also involves additional algebraic manipulations and a correction for (really the removal of) the electric field signature. Finally, we do not regard the vector neutral winds as being invariant with altitude and instead seek to estimate neutral wind profiles from the data.

The ion drifts in the *E* region are related to the electric fields and winds by the following formulas:

$$
\begin{aligned}
v_{\parallel} &= u_{\parallel} \\
\mathbf{v}_{\perp} &= \frac{\mathbf{E}\times\mathbf{B}}{B^2} r_0 + \frac{\mathbf{E}_{\perp}}{B} r_1 + \mathbf{u}\times\hat{b} r_1 + \mathbf{u}_{\perp} r_2 \\
r_0 &= \frac{1}{1+\nu^2/\Omega^2} \\
r_1 &= \frac{\nu/\Omega}{1+\nu^2/\Omega^2} \\
r_2 &= \frac{\nu^2/\Omega^2}{1+\nu^2/\Omega^2}
\end{aligned}
$$

where ν is the ion-neutral collision frequency and Ω is the ion gyrofrequency. Both of these parameters are functions of altitude to be modeled. For the aforementioned *F* region analysis, $1 \sim r_0 \gg r_1 \gg r_2$, but for the *E* region, the correct ordering is $1 > r_0 \sim r_1 \sim r_2$. In the event of multiple ion species, the correct prescription is to calculate the various r_i for each species separately and then to add the results, weighted by the fractional number density of the given species. Ion mobilities add fractionally. Below, the determination of the ion composition is considered as a separate problem.

We regard the ionospheric electric fields as being spatially invariant and use our *F* region results as the basis for their estimation. In matrix notation, the *E* region ion drifts can be related to the *F* region drifts and the neutral winds in the lower thermosphere as follows:

$$
\begin{pmatrix} v_{\parallel} \\ v_{\perp e} \\ v_{\perp n} \end{pmatrix}_E - \underbrace{\begin{pmatrix} 0 \\ v_{\perp e} r_0 + v_{\perp n} r_1 \\ v_{\perp n} r_0 - v_{\perp e} r_1 \end{pmatrix}_F}_{U} = \underbrace{\begin{pmatrix} 1 & 0 & 0 \\ 0 & r_2 & -r_1 \\ 0 & r_1 & r_2 \end{pmatrix}}_{V} \begin{pmatrix} u_{\parallel} \\ u_{\perp e} \\ u_{\perp n} \end{pmatrix} \tag{9}
$$

Here the *E* and *F* subscripts indicate *E* and *F* region ion drifts. Multiplying both sides of (9) by *S* gives, in view of (4), a relationship between the data and the underlying state parameters:

$$
\begin{pmatrix} v_l \\ v_g \end{pmatrix}_E - SU = SV \begin{pmatrix} u_{\parallel} \\ u_{\perp e} \\ u_{\perp n} \end{pmatrix}, \text{ or} \tag{10}
$$

$$
\begin{pmatrix} v'_l \\ v'_g \end{pmatrix} = Y \begin{pmatrix} u_{\parallel} \\ u_{\perp e} \\ u_{\perp n} \end{pmatrix} \tag{11}
$$

where we have defined $Y \in \mathbb{R}^{2\times 3} = SV$. In this notation, primed quantities are line of sight drift measurements in the lower thermosphere with corrections for electric fields having been made.

Whereas (10) applies for a measurement at a single time and range, we can write the result more generally for the case of data acquired at *n* times and *m* ranges independently:

$$
\begin{pmatrix} v'_{l1,1} \\ v'_{g1,1} \\ \vdots \\ v'_{lm,n} \\ v'_{gm,n} \end{pmatrix} = \underbrace{\begin{pmatrix} Y_{1,1} & & \\ & \ddots & \\ & & Y_{m,n} \end{pmatrix}}_{Z \in \mathbb{R}^{2mn\times 3mn}} \begin{pmatrix} u_{\parallel 1,1} \\ u_{\perp e1,1} \\ u_{\perp n1,1} \\ \vdots \\ u_{\parallel m,n} \\ u_{\perp em,n} \\ u_{\perp nm,n} \end{pmatrix} \tag{12}
$$

which again has the form of the equation $d = Gm$. While the problem could be inverted with the weighted-damped least squares approach, the size of the matrix *Z* is now prohibitive in view of the fact that a typical experiment may involve hundreds of ranges and time steps. Instead, we will employ an iterative method, the method of conjugate gradients least squares or CGLS, making use of the tools of sparse mathematics to improve computational performance. One of the benefits of CGLS is that it does not require any

matrix inverses or even matrix-matrix multiplies within the iterative loop. The problem is well conditioned because of the damping introduced by regularization and requires no preconditioning for convergence.

The method of normal equations again shows that the solution to (6) is given by $(G^t W_d G+\alpha^2 W_m)m = G^t W_d d$ or canonically as

$$\tilde{G}^t\tilde{G}m = \tilde{G}^t d$$
$$\tilde{G} \equiv \begin{pmatrix} W_d^{1/2} G \\ \alpha W_m^{1/2} \end{pmatrix}$$
$$\tilde{d} \equiv \begin{pmatrix} W_d^{1/2} d \\ 0 \end{pmatrix} \tag{13}$$

where the fact that the weight matrices are positive definite has been utilized in their factorizations. For this part of the analysis, the weight matrix W_m is constructed to enforce second-order Tikhonov regularization in altitude and time, penalizing spurious spatiotemporal fluctuations this time. This solution has the form $Ax = B$ required for the application of the CGLS method. Note crucially that the method is applied to the canonical equation (13) and never to the equation $\tilde{G}m = \tilde{d}$, which only holds approximately and which cannot be solved stably other than by optimization methods such as the one outlined here.

Finally, we can use R to express the vector wind estimates in geographic coordinates.

2.3. Ion Composition

It is well known that least squares fitting of the incoherent scatter spectrum cannot be used to distinguish ion composition in the lower thermosphere because of unfortunate isomorphism in the theoretical shape of the spectrum. Different combinations of atomic and molecular ions at different temperatures yield essentially identical incoherent scatter spectra. Ion neutral collisions make the uniqueness problem more severe. One approach to the problem is to use a stand-alone, empirical model for the temperature or the composition and to fit for the remaining parameters. Following *Richards et al.* [2010], we instead adopt an approach that utilizes a simple theoretical model for the composition. In the altitude region of interest, we may take $T_e = T_i$, simplifying the problem considerably.

In the lower thermosphere, we neglect transport and assume that all of the ions are in photochemical equilibrium. We consider only O^+, O_2^+, and NO^+ ions, the latter two being produced through charge exchange reactions involving the former and destroyed through dissociative recombination. Consequently, we may write the following equations balancing production (left-handed system) and loss (right-handed system):

$$\alpha \mathrm{N}[\mathrm{O}^+]\mathrm{N}[\mathrm{O}_2] = \gamma \mathrm{N}[\mathrm{O}_2^+]\mathrm{N}[\mathrm{e}^-] \tag{14}$$

$$\beta \mathrm{N}[\mathrm{O}^+]\mathrm{N}[\mathrm{N}_2] = \delta \mathrm{N}[\mathrm{NO}^+]\mathrm{N}[\mathrm{e}^-] \tag{15}$$

where α and β (γ and δ) are the rate coefficients for charge exchange (dissociative recombination). Up-to-date expressions for these coefficients can be found in *Schunk and Nagy* [2004]. Neutral density estimates are taken from the NRLMSISE-00 model [*Picone et al.*, 2002].

Equations (14) and (15) can be combined and solved algebraically for the number density fraction of the molecular ion species and, by inference, of O^+. These fractions are used in the computation of the ion mobilities needed in section 2.2. Ion-neutral collision frequencies are likewise estimated with the help of theoretical formulas taken from *Schunk and Nagy* [2004]. Since the coefficients of dissociative recombination depend on the electron temperature, this parameter must be estimated from the incoherent scatter spectra, which are fit using an iterative process that utilizes the composition and collision frequency information. The electron density, meanwhile, is estimated on the basis of the incoherent scatter power, normalized to a constant determined from ionograms recorded nearby. Since the altitudes of interest are in Arecibo's near field, we take the backscatter power to be proportional to the electron density and to be invariant with range.

3. Example Data

The event in question is presented in Figure 1, a range-time-intensity (RTI) representation of the incoherent scatter signal received with the zenith-looking line feed system at Arecibo on the evening of 8 January 2013.

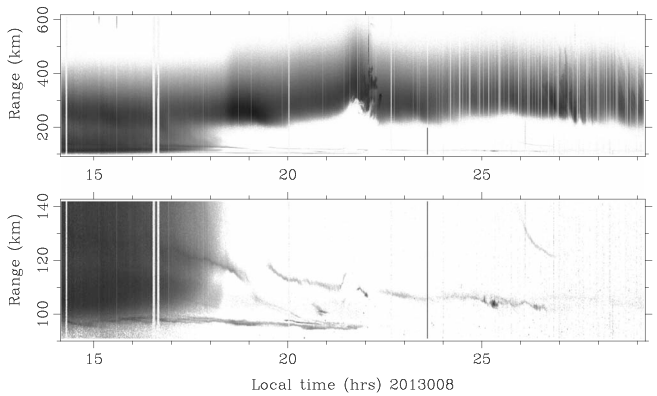

Figure 1. Range-time-intensity (RTI) plot of Arecibo line feed data for the evening of 8 January 2013. The received signal-to-noise ratio, scaled by a factor of the range squared, is plotted as a proxy for electron density on an arbitrary scale. (top) Echoes from all ranges. (bottom) Echoes from the *E* region.

The figure shows the echo signal-to-noise ratio, scaled by a factor of the square of the range and intended to serve as a proxy for electron density. The entire sample raster appears in the top half of the figure, whereas the *E* region samples are shown on an expanded range scale on the bottom half.

The data were collected under geomagnetically active conditions and are indicative of a strong midlatitude spread *F* event. A plume is visible between 2000 and 2300 LT, followed by what appear to be medium-scale traveling ionospheric disturbances (MSTIDs) after about 0230 LT the following morning. The *F* region plumes are reminiscent of what is observed at low magnetic latitudes under equatorial spread *F* (ESF) conditions. An important difference is that the plume here exhibits both locally enhanced and depleted regions of plasma (ESF is characterized predominantly by depletions.).

The *E* region echoes show the presence of two sporadic *E* layers. The first descended from about 120 km at sunset (~1800 LT) and persisted for approximately 9 h thereafter. The second maintained an altitude below 100 km and terminated by 2200 LT. Neither layer was particularly dense or particularly structured. The higher-altitude layer actually broke up around the time of the spread *F* plume and only exhibited vertical structuring and billowing in the interval between the plume and the appearance of the MSTIDs. No important coupling between the *E* and *F* layers appears to have played a role in this remarkable event.

Figure 2 shows the results of processing the signals depicted in the previous figure. Figures 2a and 2c show *E* region line of sight ion drifts computed from CLP data from the line and Gregorian feeds, respectively. Figures 2b and 2d show range-integrated *F* region line of sight ion drifts computed from MRACF data from the line and Gregorian feeds. A dashed line that runs along the bottom of Figure 2c shows the azimuth (from 0 to 360°) of the Gregorian feed pointing. The passage of the midlatitude spread *F* plume around 2200 LT is clearly evident in the MRACF data. Structuring in the Gregorian MRACF drifts signal is evidence of the large contribution of horizontal motion to the line of sight drifts observed obliquely.

Close examination of Figure 2a shows echoes with small Doppler shifts below about 115 km, red shifts between about 115 and 125 km, and blue shifts above that altitude. We can interpret these three zones as zones where the ion drifts are dominated by neutral winds, Pedersen drifts, and Hall drifts, in ascending order. (The transition from Pedersen to Hall drift signifies the altitude where the ion-neutral collision frequency matches the ion gyrofrequency.) This implies that the electric field should have northward and westward perpendicular-to-B components, or westward and southward perpendicular-to-B drift, before 1800 LT.

Even closer examination of Figure 2c around 100 km altitude prior to 1800 LT reveals strong variations in the line of sight drifts with altitude and azimuth. The entire data record and this area in particular is indicative of vertical shear in the horizontal ion drift velocity, itself indicative of strong wind shear.

Figure 2e shows the temperatures, fits to the line feed CLP autocorrelation functions performed iteratively with the composition model from section 2.3. While the isotherms are approximately horizontal in the panel, significant perturbations are evident, and some of the mixing suggested in the RTI plots in Figure 1 is also suggested by the temperatures. Note that as the sporadic *E* layers are likely metallic in composition, we do not expect our fitting procedure to yield accurate temperature estimates within them or the strata from which they emerged.

The results of the inversion of the MRACF drifts described in section 2.1 are plotted in Figure 2f. The model prediction error associated with these estimates is small; i.e., the line of sight drifts predicted by these

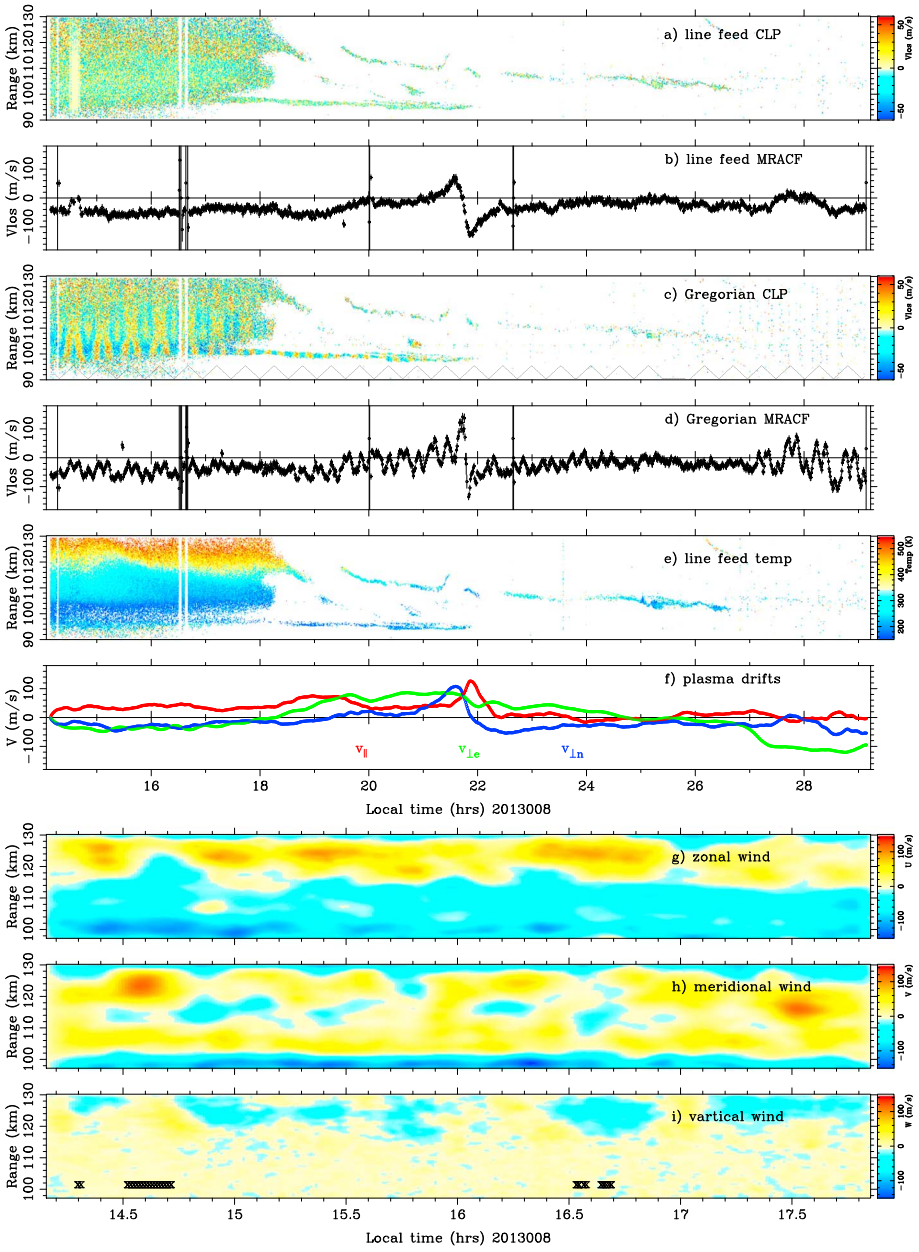

Figure 2. Results from the Arecibo winds analysis. (a and c) Line of sight ion drifts measured with the coded long-pulse technique using the line and Gregorian feeds, respectively. (b and d) Averaged *F* region line of sight plasma drifts measured by the line and Gregorian feeds, respectively. (e) Temperature estimates from the line feed data. (f) Derived *F* region plasma drifts. (g–i) Derived zonal, meridional, and vertical wind speed profiles, respectively. Note that range is equal to altitude for line feed data only.

estimates resemble the data closely. At the same time, regularization presents severe artifacts in these estimates associated with beam swinging that would otherwise occur. As expected, the estimates suggest westward and southward perpendicular drifts before 1800 LT accompanied with positive parallel (down the field line) drifts that combine to give rise to the descent of the *F* layer. Descent continues until about 2100 LT, when the perpendicular drifts reverse to northward and overcome the downward parallel motion. Just before 2200 LT, the perpendicular drifts turn southward again, and the parallel drifts intensify, leading to the rapid descent and collapse of the *F* layer. The midnight collapse is a regular and well-documented feature of the midlatitude ionosphere [*Gong et al.*, 2012]. In this case, it was dramatic and accompanied by convective plasma instability. Not only the *F* layer but also the upper sporadic *E* layer was affected.

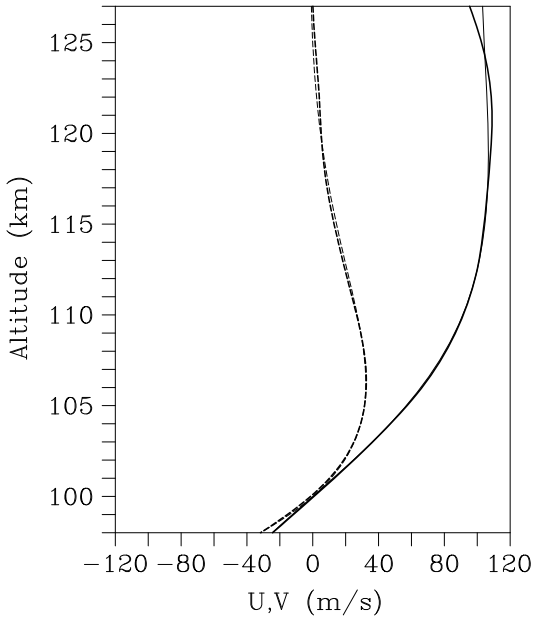

Figure 3. Truth test of the data inversion algorithm. Solid and dashed lines represent zonal and meridional winds, respectively. The light lines are the truth model at one instant in time, and the heavy lines are the wind estimates recovered by our data inversion process at the corresponding time.

Between 1800 and 2400 LT and again after 0200 LT, the eastward perpendicular drifts were large. It is noteworthy that the period of strong westward drifts after 0200 LT was coincident with the appearance of MSTIDs.

Finally, Figures 2g and 2h show horizontal wind estimates for the period between 1400 and 1800. The estimates were derived using the procedure outlined in section 2.2. Plotter symbols ("X") denote regions of poor data quality, which gave rise to somewhat spurious results.

For iterative methods such as CGLS, there is no straightforward way to propagate errors in the measured quantities through to uncertainties in the model parameters. We have therefore made use of a Monte Carlo approach, estimating ion drifts and neutral winds for a statistical ensemble of data vectors generated from the original data through the addition of independent Gaussian random noise. The noise was generated in accordance with the error estimates calculated for the ISR data. The ensemble had 1000 members.

We find that the individual components of the ion drift estimators ($v_{\|}$, $v_{\perp e}$, $v_{\perp n}$) have standard deviations less than 5 m/s. The neutral wind component (u, v) estimators also have standard deviations less than 5 m/s, except for the vertical components (w), which have standard deviations less than 1 m/s. We have not plotted the error bars since they are small and would be difficult to discern. Their computation was notably much more numerically expensive than the data inversion itself.

The significance of the small model uncertainties should not be overemphasized. These uncertainties represent the level of fluctuation that can be expected to arise in the model parameters from independent fluctuations in the input data. The effect of regularization is to suppress the impact of data fluctuations, however, in the maintenance of regular model values. Regularization improves the accuracy of the model estimates only to the degree that the implicit prior information is itself accurate, something beyond the ability of conventional error propagation to determine.

Lastly, we have performed a simple truth test of the data inversion procedure. We specified height- and time-dependent profile shapes for the zonal and meridional winds, converted the profiles to the preferred coordinate system using (2), simulated data consistent with the profiles using (3), and then performed the inversion as specified above in an attempt to recover the truth model. For simulated data error estimators, we used the same values as for the actual data. The truth model chosen for the calculation was a simple Ekman spiral, rotating about the vertical axis with a 1 h period.

The instantaneous results of the truth test are shown in Figure 3. The agreement between the truth model and the recovered model is very good except possibly near the vertical boundaries. The agreement is equally good at all times except at the initial and final boundaries.

The ion drift and neutral wind profiles shown in Figure 2 can be compared directly with equivalent parameters estimated at Arecibo by *Harper et al.* [1976] and *Harper* [1977]. Whereas the magnitudes of the ion drifts and neutral winds we find are comparable, they are reported here with a considerably higher cadence (The Harper parameters were estimated at half-hourly intervals.). We are therefore not restricted, for example, to tidal mode analyses but can also explore behaviors associated with gravity waves and dynamic and other neutral instabilities. The cadence of our results is comparable to those of *Fritts and Janches* [2008], *Zhou et al.* [2011], and *Gong et al.* [2012]. Those studies, however, did not involve full vector parameter estimation.

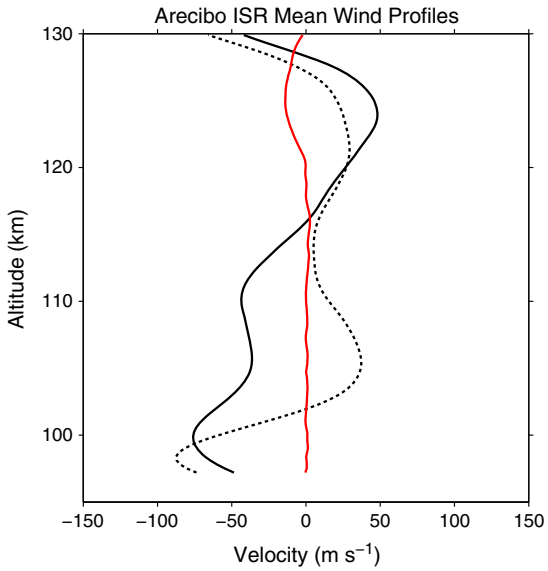

Figure 4. Mean zonal (solid black line), meridional (dotted black line), and vertical velocity (solid red line) profiles obtained from the analysis of the incoherent scatter radar drift data for the approximately 4 h period.

4. Derived Wind Profiles

The previously published analyses of the *E* region winds obtained from incoherent scatter radar measurements at Arecibo have used the standard approach of solving the ion momentum equation for the zonal and meridional neutral wind components as a function of altitude in the height range from approximately 90 to 120 km [see, e.g., *Zhou et al.*, 1997]. In a different experimental setup that was used in a much more limited extent, *Zhou* [2000] used the Arecibo incoherent scatter radar with a vertically pointing beam to obtain the vertical neutral winds in the altitude range from approximately 65 to 95 km. The approach described in the previous section provides all three components of the neutral winds between 95 and 130 km altitude with a height resolution of 300 m and a time resolution of a minute or less.

The wind profile analysis technique described in the previous section and illustrated by Figures 2a–2i is only viable when there is sufficient plasma in the *E* region to provide good signal-to-noise ratios for the measurements at those altitudes. Although the observation period extended from approximately 1400 LT to 0500 LT on the following day, the period with large *E* region plasma densities was limited to early part of the observation period, i.e., the daylight hours. The zonal and meridional neutral wind components for the first 4 h of the observations are shown in Figures 2h and 2i.

The horizontal winds exhibit large amplitudes, quasi-periodic variations with altitude, and strong shears in the altitude region of interest. The winds are characterized by vertical wavelengths of about 20 km and slow downward propagation. This is true of both the zonal and the meridional component. The largest amplitudes and strongest shears occur at the bottom of the *E* layer, around 100 km, which is consistent with the characteristics broadly evident in Figure 2c. Less evident in Figure 2c but present nonetheless is a region of strong shear higher in altitude, around 125 km. It is noteworthy that from these two altitude regions emerged the sporadic *E* layers described earlier.

The mean winds for the period are shown in Figure 4, including the zonal (solid line), meridional (dotted line), and vertical (red line) wind profiles. The largest wind speeds occur between 95 and 100 km. The general rotation of the horizontal wind vector is from southwest to northwest to northeast with height, i.e., generally clockwise with height. The mean vertical winds are small, close to zero, below 120 km but show larger values above that height, with a mean value approaching 10 m s^{-1} near 125 km.

All three components of the winds are plotted in Figure 5 for the period from 1400 to 1800 LT. In the figure, 1 h corresponds to 100 m s^{-1}, and perturbation winds with that magnitude are evident throughout the altitude range above 100 km. There are no independent neutral wind measurements that can be compared to the derived winds, but the derived zonal winds show the downward phase progression for the perturbation winds that would be expected for gravity waves propagating through the region. Notable examples are found in the altitude range between 110 and 120 km between 1500 and 1600 LT and between 97 and 103 km during the interval from 1400 to 1530 LT. In general, the profiles show large-amplitude perturbation winds with a general downward phase progression trend and features that persist for less than one and a half wave periods.

The meridional perturbation winds shown in Figure 5 have features that are generally similar to those seen in the zonal perturbations. Qualitatively, it appears that for corresponding features in the zonal and meridional winds, the zonal perturbation leads the meridional perturbation in phase, corresponding to a counterclockwise rotation of the wind vector with height.

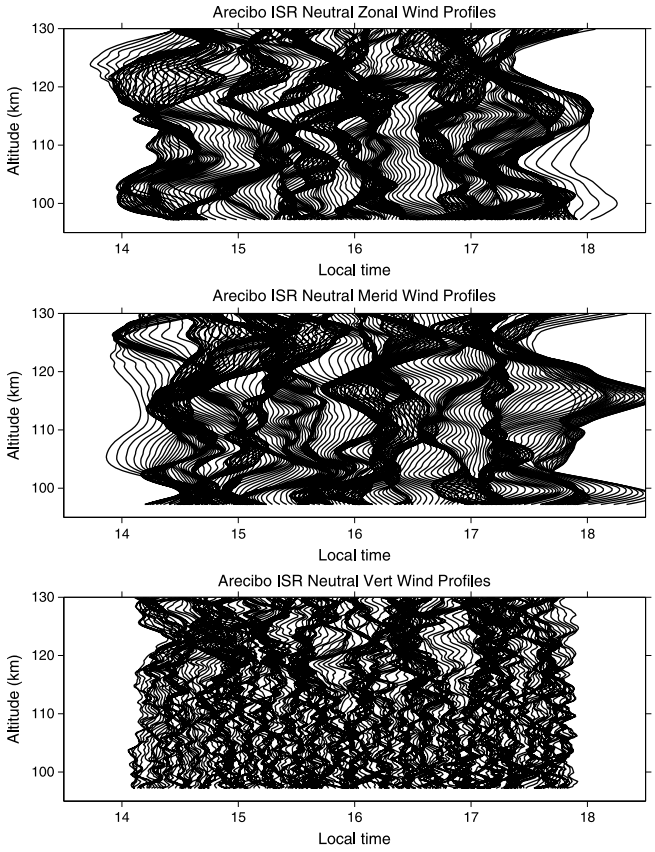

Figure 5. Wind deviations from the mean for the 4 h period. (top) Zonal deviations. (middle) Meridional deviations. (bottom) Vertical deviations. One hour corresponds to 100 m s^{-1}.

The vertical wind perturbations are shown in Figure 5 (bottom) in the same format as Figure 5 (top and middle). The curves show a significant increase in the perturbation amplitudes above 110 km, with the same general features persisting for a significant fraction of an hour or more, consistent with the features seen in the two horizontal wind components. *Larsen and Meriwether* [2012] have summarized the available thermospheric vertical wind data obtained from radar, optical, satellite, and rocket techniques. The vertical velocities are critical for understanding transport and vertical coupling in the thermosphere, as well as the interaction between the neutrals and plasma. In spite of the great interest in the parameter, relatively few measurements are available because of the difficulty of making such measurements. One of the conclusions drawn from the overview of the available data is that all the measurements are consistent in showing that large vertical wind speed are common at all latitudes and over broad altitude ranges in the thermosphere. The vertical velocities obtained from the Arecibo radar data show similar features, namely, vertical velocity magnitudes that are generally 10 m s^{-1} or greater and persist for periods of an hour or longer. The vertical winds shown here furthermore show a transition in the behavior near 110 to 115 km, with smaller amplitude and more rapid variations below the transition and larger and slower variations above. Larsen and Meriwether discussed the fact that lidar vertical wind measurements, extending up to 100 km, do not show the characteristics that appear to be typical of the thermospheric vertical velocities, implying that there is a transition somewhere close to 100 km altitude. The transition seen here may be evidence of that.

5. Significance and Future Work

The objective of this work is to optimize the utilization of the Arecibo radio telescope, the most sensitive of the incoherent scatter radars, for wind profile measurements in the MALT region. This has been done by replacing multiple fixed-azimuth data with data collected while the azimuth is varying continuously. The problem is mixed determined, and statistical inverse methods are required to overcome problems associated with the existence, uniqueness, and stability of wind profile solutions. The problem is linear and has

been addressed here using second-order Tikhonov regularization, a conjugate gradient least squares solver, and sparse matrix math.

The slew rate for the Arecibo feed system is 25°/min or 90°/3.6 min. A fixed-azimuth experiment designed to spend more time acquiring data in either cardinal direction than it does in beam swinging therefore has a practical cadence of no more than one solution every 10.8 min. However, this interval is comparable to or longer than the Brunt-Väisälä period in the MALT region. Much of the fine structure in the wind profiles is consequently excluded by fixed-azimuth experiments. The analysis described in this paper produced wind profiles every minute. This figure is derived from the cadence of the nominal International World Day mode employed at Arecibo and the rate at which the MRACF and CLP modes is normally interleaved. The effective cadence of the experiment is limited by the amount of regularization used, a parameter adjusted in this case to limit the variance in the profiles (in altitude and time) without introducing significant model projection error. The evidence of Figure 2 is that the method permits variations in the wind profiles on time scales of 5 min or less.

Finely resolved neutral wind measurements in the MALT region are required in view of the predominant wind characteristics that are fundamentally nontidal [e.g., *Harper*, 1977; *Larsen*, 2002; *Sherman and She*, 2006; *Liu*, 2007]. The region is the site of wave breaking and wave-mean flow interactions as well as a number of viable instabilities. This is a frontier research area in need of incisive experimental tools.

A number of improvements to the basic methodology described here are possible. A simple one would be to limit the azimuth scans to a single quadrant. This would reduce by a factor of 4 the size of the volume being probed by the radar, making the assumption of spatial homogeneity more likely to be satisfied.

Another improvement involves combining *F* region plasma drift and *E* region neutral wind estimation into a single optimization problem. We expect the vertical neutral winds to be relatively small, and this imposes additional constraints on the electric fields, as even small errors in the latter give rise to large deviations in the former. More accurate electric field estimates, in turn, translate to more accurate horizontal wind estimates. The combination of the two inverse problems into one, combined with the addition of a small penalty on the size of the vertical wind estimates, constitutes an important potential refinement.

The altitude range between 90 and 130 km is a critical region of the atmosphere that includes the transition from a neutral atmosphere dominated by neutral dynamics to a partially ionized atmosphere with strong electrodynamic effects. The neutrals are still the dominant drivers in that part of the atmosphere, but the plasma densities are large enough so that the ionization can create feedback in response to the neutral forcing that affects the dynamics of the neutrals. A critical problem in trying to understand the dynamics of the region has been the lack of high-resolution wind measurements across the altitude range where much of the important interaction between ions and neutrals occurs. Lidars and radars using coherent scatter from neutral turbulence fluctuations generally only provide coverage up to altitudes of 100 km or slightly higher. Chemical release measurements from rockets can provide measurements over a broad altitude range with good height resolution, but the expense and logistical complexity associated with the rocket launches make it difficult to make more than one or two wind profile measurements on a given night. Satellite measurements provide broad spatial coverage but generally have poor height resolution that makes the measurements less than ideal for detailed studies of lower *E* region electrodynamics. The technique described here offers the potential to provide detailed measurements of all three wind components with time resolution significantly better than the Brunt-Väisälä period and height resolution good enough to resolve the narrow layers that are a characteristic of the lower *E* region. Although the basic idea behind the technique, namely, using the ion momentum equations to infer the neutral winds, has been used since at least the 1970s, the regularization technique opens new possibilities for expanding the technique and making the ISR a much more capable neutral wind instrument. An obvious priority for the near future is to find a way to validate the wind estimates obtained with the technique described here.

Acknowledgments

This work was supported by awards AGS-1007568 and AGS-1007539 from the National Science Foundation to Cornell University and Clemson University. The Arecibo Observatory is part of the National Astronomy and Ionosphere Center which is operated under a cooperative agreement with the National Science Foundation.

Robert Lysak thanks the reviewers for their assistance in evaluating this paper.

References

Aponte, N., M. J. Nicolls, S. A. González, M. P. Sulzer, M. C. Kelley, E. Robles, and C. A. Tepley (2005), Instantaneous electric field measurements and derived neutral winds at Arecibo, *Geophys. Res. Lett.*, *32*, L12107, doi:10.1029/2005GL022609.

Aster, R. C., B. Borchers, and C. H. Thurber (2005), *Parameter Estimation and Inverse Problems*, Elsevier, New York.

Behnke, R. A., and R. M. Harper (1973), Vector measurements of *F* region ion transport at Arecibo, *J. Geophys. Res.*, *78*, 8222–8234, doi:10.1029/JA078i034p08222.

Behnke, R. A., and H. Kohl (1974), The effect of neutral winds and electric fields on the ionospheric F_2-layer over Arecibo, *J. Atmos. Terr. Phys.*, *36*, 325–333.

Brum, C. G. M., C. A. Tepley, J. T. Fentzke, E. Robles, P. T. Santos, and S. A. Gonzalez (2012), Long-term changes in the thermospheric neutral winds over Arecibo: Climatology based on over three decades of Fabry-Perot observations, *J. Geophys. Res.*, *117*, A00H14, doi:10.1029/2011JA016458.

Burnside, R. G., R. A. Behnke, and J. G. Walker (1983), Meridional neutral winds in the thermosphere at Arecibo: Simultaneous incoherent scatter and airglow observations, *J. Geophys. Res.*, *88*, 3181–3189.

Chu, X., C. S. Gardner, and S. J. Franke (2005), Nocturnal thermal structure of the mesosphere and lower thermosphere region at Maui, Hawaii (20.7°N), and Starfire Optical Range, New Mexico (35°N), *J. Geophys. Res.*, *110*, D09S03, doi:10.1029/2004JD004891.

Fritts, D. C., and D. Janches (2008), Dual-beam measurements of gravity waves over Arecibo: Reevaluation of wave structure, dynamics, and momentum fluxes, *J. Geophys. Res.*, *113*, D05112, doi:10.1029/2007JD008896.

Fukao, S., T. Sato, N. Yamasaki, R. M. Harper, and S. Kato (1982), Winds measured by a UHF Doppler radar and rawinsondes—Comparisons made on 26 days (August–September 1977) at Arecibo, Puerto Rico, *J. Appl. Met.*, *21*, 1357–1363.

Fukao, S., Y. Maekawa, T. Sato, and S. Kato (1985), Fine-structure in mesospheric wind fluctuations observed by the Arecibo UHF Doppler radar, *J. Geophys. Res.*, *90*, 7547–7556.

Gong, Y., Q. H. Zhou, S. D. Zhang, N. Aponte, M. Sulzer, and S. Gonzalez (2012), Midnight ionosphere collapse at Arecibo and its relationship to the neutral wind, electric field, and ambipolar diffusion, *J. Geophys. Res.*, *117*, A08332, doi:10.1029/2012JA017530.

Harper, R. M. (1977), Tidal winds in the 100- to 200-km region at Arecibo, *J. Geophys. Res.*, *82*, 3243–3250.

Harper, R. M., R. H. Wand, C. J. Zamlutti, and D. T. Farley (1976), *E* region ion drifts and winds from incoherent scatter measurements at Arecibo, *J. Geophys. Res.*, *81*, 25–35, doi:10.1029/JA081i001p00025.

Huang, C. M., S. D. Zhang, Q. H. Zhou, F. Yi, and K. M. Huang (2012), Atmospheric waves and their interactions in the thermospheric neutral wind as observed by the Arecibo incoherent scatter radar, *J. Geophys. Res.*, *117*, D19105, doi:10.1029/2012JD018241.

Hysell, D. L., E. Nossa, M. F. Larsen, J. Munro, M. P. Sulzer, N. Aponte, and S. A. González (2009), Sporadic *E* layer observations over Arecibo using coherent and incoherent scatter radar: Assessing dynamic stability in the lower thermosphere, *J. Geophys. Res.*, *114*, A12303, doi:10.1029/2009JA014403.

Larsen, M. F. (2002), Winds and shears in the mesosphere and lower thermosphere: Results from four decades of chemical release wind measurements, *J. Geophys. Res.*, *107*(A8), 1215, doi:10.1029/2001JA000218.

Liu, H. L. (2007), On the large wind shear and fast meridional transport above the mesopause, *Geophys. Res. Lett.*, *34*, L08815, doi:10.1029/2006GL028789.

Maekawa, Y., T. Aso, J. Rottger, P. Czechowsky, R. Ruster, G. Schmidt, I. Hirota, R. F. Woodman, and S. Kato (1986), A cooperative synchronous observation of winds and tides in the tropical lower stratosphere and mesosphere using VHF radars at Jicamarca and Arecibo, *J. Geom. Geoel.*, *38*, 81–97.

Maekawa, Y., S. Fukao, I. Hirota, M. P. Sulzer, and S. Kato (1987), Some further results on long-term mesospheric and lower thermospheric wind observations by the Arecibo UHF radar, *J. Atmos. Terr. Phys.*, *49*, 63–71.

Mathews, J. D., M. P. Sulzer, C. A. Tepley, R. Bernard, J. L. Fellous, M. Glass, M. Massebeuf, S. Ganguly, R. M. Harper, and R. A. Behnke (1981), A comparison between Thomson scatter and meteor radar wind measurements in the 65–105 km altitude region at Arecibo, *Planet. Space Sci.*, *29*, 341–348.

Menke, W. (1984), *Geophysical Data Analysis: Discrete Inverse Theory*, Academic, New York.

Nygrén, T., A. T. Aikio, R. Kuula, and M. Voiculescu (2011), Electric fields and neutral winds from monostatic incoherent scatter measurements by means of stochastic inversion, *J. Geophys. Res.*, *116*, A05305, doi:10.1029/2010JA016347.

Picone, J. M., A. E. Hedin, D. P. Drob, and A. C. Aikin (2002), NRLMSISE-00 empirical model of the atmosphere: Statistical comparisons and scientific issues, *J. Geophys. Res.*, *107*(A12), 1468, doi:10.1029/2002JA009430.

Richards, P. G., D. Bilitza, and D. Voglozin (2010), Ion density calculator (IDC): A new efficient model of ionospheric ion densities, *Radio Sci.*, *45*, RS5007, doi:10.1029/2009RS004332.

Roper, R. G., G. W. Adams, and J. W. Brosnahan (1993), Tidal winds at mesopause altitudes over Arecibo (18°N, 67°W), 5–11 April 1989 (AIDA 89), *J. Atmos. Terr. Phys.*, *55*, 289–312.

Rottger, J., P. Czechowsky, and G. Schmidt (1981), First low-power VHF radar observations of tropospheric, stratospheric and mesospheric winds and turbulence at the Arecibo Observatory, *J. Atmos. Terr. Phys.*, *43*, 789–800, doi:10.1016/0021–9169(81)90,056–8.

Rottger, J., P. Czechowsky, R. Ruster, and G. Schmidt (1983), VHF radar observations of wind velocities at the Arecibo Observatory, *J. Geophys.*, *52*, 34–49.

Santos, P. T., C. G. M. Brum, C. A. Tepley, N. Aponte, S. A. Gonzalez, and E. Robles (2011), Using incoherent scatter radar to investigate the neutral wind long-term trend over Arecibo, *J. Geophys. Res.*, *116*, A00H13, doi:10.1029/2011JA016514.

Schunk, R. W., and A. F. Nagy (2004), *Ionospheres: Physics, Plasma Physics, and Chemistry*, Cambridge Univ. Press, Cambridge, U. K.

Sherman, J. P., and C. Y. She (2006), Seasonal variation of mesopause region wind shears, convective and dynamic instabilities above Fort Collins, CO: A statistical study, *J. Atmos. Sol. Terr. Phys.*, *68*, 1061–1074.

Sulzer, M. P. (1986a), A phase modulation technique for a sevenfold statistical improvement in incoherent scatter data-taking, *Radio Sci.*, *21*, 737–744, doi:10.1029/RS021i004p00737.

Sulzer, M. P. (1986b), A radar technique for high range resolution incoherent scatter autocorrelation function measurements utilizing the full average power of klystron radars, *Radio Sci.*, *21*, 1033–1040.

Sulzer, M. P., N. Aponte, and S. A. González (2005), Application of linear regularization methods to Arecibo vector velocities, *J. Geophys. Res.*, *110*, A10305, doi:10.1029/2005JA011042.

Tarantola, A. (1987), *Inverse Theory*, Elsevier, New York.

Tepley, C. A., E. Robles, R. Garcia, P. T. Santos, C. M. Brum, and R. G. Burnside (2011), Directional trends in thermospheric neutral winds observed at Arecibo during the past three solar cycles, *J. Geophys. Res.*, *116*, A00H06, doi:10.1029/2010JA016172.

Tsuda, T., K. Hirose, S. Kato, and M. P. Sulzer (1985), Some findings on correlation between the stratospheric echo power and the wind shear observed by the Arecibo UHF radar, *Radio Sci.*, *20*, 1503–1508.

Vasseur, G. (1969), Vents dans la thermosphere dduits des mesures par diffusion de Thomson, *Ann. Geophys.*, *25*, 517–527.

Zhao, Y., A. Z. Liu, and C. S. Gardner (2003), Measurements of atmospheric stability in the mesopause region at Starfire Optical Range, NM, *J. Atmos. Sol. Terr. Phys.*, *65*, 219–232.

Zhou, Q. H. (2000), Incoherent scatter radar measurements of vertical winds in the mesosphere, *Geophys. Res. Lett.*, *27*, 1803–1806.

Zhou, Q. H., and Y. T. Morton (2006), A case study of mesospheric gravity wave momentum flux and dynamical instability using the Arecibo dual beam incoherent scatter radar, *Geophys. Res. Lett.*, *33*, L10802, doi:10.1029/2005GL025608.

Zhou, Q. H., M. P. Sulzer, and C. A. Tepley (1997), An analysis of tidal and planetary waves in the neutral winds and temperature observed at low-latitude *E* region heights, *J. Geophys. Res.*, *102*, 11,491–11,506.

Zhou, Q. H., Y. T. Morton, C. M. Huang, N. Aponte, M. Sulzer, and S. Gonzalez (2011), Incoherent scatter radar observation of E-region vertical electric field at Arecibo, *Geophys. Res. Lett.*, *38*, L01101, doi:10.1029/2010GL045549.